RSC Advances

PAPER

View Article Online
View Journal | View Issue

Cite this: *RSC Adv.*, 2021, **11**, 22287

Fabrication and catalytic performance of a novel tubular PMIA/Ag@RGO nanocomposite nanofiber membrane†

Mingxing Chen, *[a] Lianying Wei,[a] Wei Zhang,[a] Chun Wang*[b] and Changfa Xiao [b]

Received 12th May 2021
Accepted 9th June 2021

DOI: 10.1039/d1ra03707b

rsc.li/rsc-advances

A novel tubular poly(*m*-phenylene isophthalamide) (PMIA) nanofiber membrane decorated with Ag nanoparticles was fabricated *via* a simple method in this study. First, Ag@RGO nanocomposites were prepared *via* a mussel-inspired method. Then, a tubular PMIA/Ag@RGO nanocomposite nanofiber membrane (T-PMIA/Ag@RGO NNM) was prepared by adding Ag@RGO nanocomposites to the electrospining solution. In particular, hollow braided rope was used as the collector and reinforcement during the electrospinning process. T-PMIA/Ag@RGO NNM exhibits an excellent catalytic efficiency as most of the Ag nanoparticles were exposed to the surface of the nanofiber and because of the fast mass transfer in continuous catalysis process. T-PMIA/Ag@RGO NNM can be easily recycled from the reaction solution and exhibits good reusability. The degradation rate for 4-NP could still remain 98.7% after ten consecutive cycles. The results might advance the real applications of the nanofiber membrane in the continuous catalysis process.

1. Introduction

Noble metal nanoparticles (NPs) have attracted considerable attention for their unique properties and broad applications in catalysis,[1–3] antibacterial,[4–6] surface enhanced Raman scattering[7–10] and chemical sensing.[11,12] It is known that noble metal NPs tend to aggregate due to the high surface energy, leading to the formation of larger particles and a huge reduction in activity. Moreover, the recyclability of noble metal NPs is also poor due to its nano size. These are significant challenges for the applications of noble metal NPs.

In order to solve these problems, some efforts have been done. There are two common strategies to solve the agglomeration of noble metal NPs. One is surface modification with small molecular or polymeric ligands. Another effective strategy is to immobilize them on various supports such as polymers,[13,14] carbon materials[15–18] and metal–organic frameworks.[19–21] As a widely used two-dimensional material, graphene oxide (GO) is known to be a superior substrate due to the functional groups such as hydroxyl, carbonyl, and epoxy, which can act as nucleation sites for the loading of noble metal nanoparticles.[22,23] Thus, numerous researchers have paid much attention to prepare noble metal NP/GO nanocomposites and studied their performance.[23–27] As a facile and environmentally friendly method for preparing noble metal NPs/GO nanocomposites, the mussel-inspired modification of graphene oxide for preparing noble metal NPs/GO nanocomposites has been used widely in recent years.[28–32] Although the noble metal NPs/GO nanocomposite shows superior performance to that of bulk noble metal NPs, the recyclability of the nanocomposite is still poor.

As a unique nanomaterial, nanofibers are widely used as the matrix to improve the recyclability of noble metal NPs due to their nanometric diameter and large surface area.[33] There are two common methods for preparing noble metal NPs/nanofiber composites. One is assembling noble metal NPs on the surface of nanofibers. In a previous study, several noble metal NPs have been coated successfully on the surface of nanofibers, such as Ag/PVDF nanofibers,[34] Ag/PAN nanofibers,[35] Au/PAN nanofibers,[36] Au/PVA nanofibers[37] and Au/CA nanofibers.[38] Although these noble metal NPs/polymer nanofibers display good stability and recyclability, the prepared process is little complicated. The other common method is blending noble metal NPs or their precursors with a polymer solution, and then, nanofibers are prepared by the electrospinning process.[11,39–41] Although it is an easy way to fabricate noble metal NPs/nanofiber composites, the activity of noble metal NPs/nanofiber composites may be poor as some of noble metal NPs are inside the nanofibers as their diameter is much smaller than that of the nanofibers. Hence, another method needs to be developed to fabricate noble metal NPs/nanofiber composites.

[a]*School of Textile and Garment, Hebei Province Technology Innovation Center of Textile and Garment, Hebei Key Laboratory of Flexible Functional Materials, Hebei University of Science and Technology, No. 26, Yuxiang Road, Shijiazhuang, 050018, China. E-mail: mxchen1990@163.com; bcmdy@163.com; Tel: +86 0311-81668828; +86 0311-81668817*

[b]*School of Textiles and Fashion, Shanghai University of Engineering Science, No. 333, Longteng Road, Shanghai, 201620, China*

† Electronic supplementary information (ESI) available. See DOI: 10.1039/d1ra03707b

Furthermore, the continuous catalysis process has attracted considerable attention recently as the catalytic efficiency is higher during this process.[3,42–48] However, the mechanical properties of nanofiber membranes are usually poor; therefore, they are often used in the static catalytic process. Their usage in the continuous catalysis process is still a challenge. In our previous study, an Ag/PMIA nanofiber membrane[49] and Ag/PVDF-HFP nanofiber membrane,[50] which can be used in the continuous catalysis process and showed higher catalytic efficiency, were prepared. However, the preparation method was somewhat complicated. Therefore, there is an urgent need to develop a simple method to prepare a nanofiber membrane, which can be used in the continuous catalysis process.

In this study, novel tubular PMIA/Ag@RGO nanocomposite nanofiber membranes (T-PMIA/Ag@RGO NNMs), which could be used in the continuous catalysis process, were prepared *via* a simple electrospining process. PMIA was selected as the polymer to fabricate the nanofibers due to its excellent thermal stability and mechanical property.[51–53] First, the Ag@RGO nanocomposite was prepared *via* a mussel-inspired method. Then, the Ag@RGO nanocomposite was added into the PMIA polymer solution to prepare T-PMIA/Ag@RGO NNM using hollow braided rope as the collector. The majority of Ag nanoparticles were not covered by the PMIA nanofiber as the diameter of Ag@RGO nanosheets was larger than that of the nanofiber. The morphology, XRD, XPS and mechanical property of T-PMIA/Ag@RGO NNM were characterized. Lastly, the catalytic properties of the tubular PMIA/Ag@RGO nanofiber membrane were tested under continuous and static catalysis modes. The results demonstrate a high catalytic enhancement of T-PMIA/Ag@RGO NNMs in the continuous catalysis process.

2. Experimental section

2.1 Materials

A PMIA staple was supplied by SRO Aramid Co., Ltd. (Huaian, China). The hollow braided rope was purchased from Tianjin Boanxin Co., Ltd. (China). Dopamine hydrochloride (DA) and tris-(hydroxymethyl)aminomethane (Tris) were purchased from J&K Scientific Ltd. (Beijing, China). GO was purchased from Suzhou Tanfeng Graphene Science and Technology Co., Ltd. (Suzhou, China). Silver nitrate ($AgNO_3$) was bought from Tianjin Yingda Rare Chemical Reagents Factory (Tianjin, China). Dimethylacetamide (DMAc), lithium chloride (LiCl), 4-nitrophenol (4-NP) and sodium borohydride ($NaBH_4$) were purchased from Tianjin Kermel Chemical Reagent Co., Ltd. (Tianjin, China).

2.2 Preparation of the Ag@RGO nanocomposite

The Ag@RGO nanocomposite was prepared *via* the mussel-inspired method. First, 0.5 g of GO was dispersed into 1000 ml of tris–HCl (10 mM, pH = 8.5) buffer solution. Then, 2 g of dopamine hydrochloride was added into the solution. After that, the mixture was stirred for 24 h at room temperature. The product (named PDA@RGO) was collected *via* centrifugation and rinsed with water several times. Second, PDA@RGO was dispersed into a 1000 ml deionized water solution. After adding 5 g $AgNO_3$, the mixture was stirred for 24 h at room temperature without light. The product (named Ag@RGO) was also collected by centrifugation and rinsed with water several times. Then, the Ag@RGO nanocomposite was freeze-dried and stored for use.

2.3 Preparation of T-PMIA/Ag@RGO NNM

To prepare PMIA/Ag@RGO composite spinning solutions, the Ag@RGO nanocomposite and LiCl was added into the DMAc solution and sonicated for 10 min, followed by adding PMIA. Then, the mixture was stirred continuously for 5 h under 70 °C. The composition of the electrospining solution is listed in Table 1. Then, T-PMIA/Ag@RGO NNM was prepared using the electrospinning unit. The parameters of the electrospinning process were listed in Table S1.† After that, the obtained nanofiber membrane was placed in a vacuum oven at 60 °C for 10 h to remove the residual solvent. The schematic of preparing T-PMIA/Ag@RGO NNM is shown in Fig. 1 and S1.†

2.4 Characterization

A scanning electron microscope (SEM, S4800, Hitachi, Japan) and transmission electron microscope (TEM) (H7650, Hitachi, Japan) were used to observe the morphologies of samples. The elemental composition of T-PMIA/Ag@RGO NNM was investigated *via* energy dispersive X-ray spectroscopy (EDX) (APOLLO XL, EDAX, USA). An X-ray photoelectron spectrometer (XPS) (K-alpha, Thermo Scientific, USA) was used to determine the surface composition of the samples. The X-ray diffraction results were obtained using Cu-Ka radiation on an X-ray diffractometer (D8 Advance, Bruker, Germany).

2.5 Catalytic test of T-PMIA/Ag@RGO NNM

The catalytic performance of T-PMIA/Ag@RGO NNM was tested by performing the reduction of 4-nitrophenol (4-NP) to 4-aminophenol (4-AP) in water at room temperature. First, 5 mg 4-NP was added into 500 ml deionized water for preparing the 4-NP aqueous solution. Then, a certain amount of $NaBH_4$ was added to the 4-NP aqueous solution as the reducing agent. For the

Table 1 The composition of the PMIA electrospining solution

Membrane ID	Ag@RGO (wt%)	PMIA (wt%)	LiCl (wt%)	DMAc (wt%)
PMIA	0	12	2	86
PMIA/Ag@RGO0.2	0.2	12	2	85.8
PMIA/Ag@RGO0.6	0.6	12	2	85.4
PMIA/Ag@RGO1.0	1	12	2	85

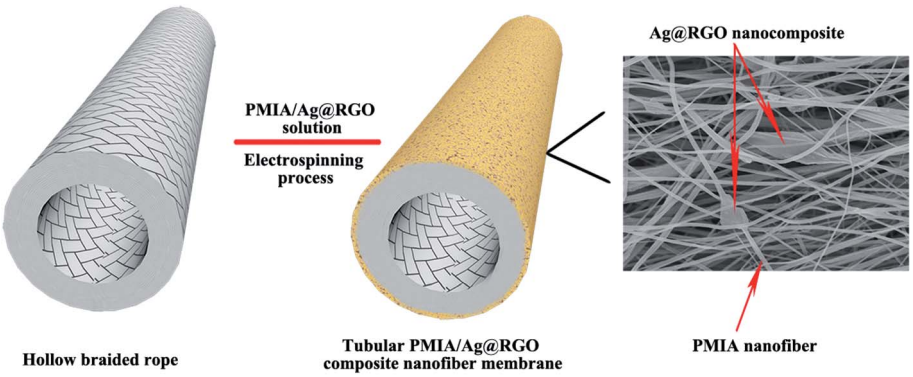

Fig. 1 The schematic of the preparation of T-PMIA/Ag@RGO NNM.

static catalysis, T-PMIA/Ag@RGO NNM was immersed into the feed solution directly (shown in Fig. S2†). The reaction process was supervised by UV-Vis spectrometry (TU1810PC, China) at room temperature. The continuous catalysis process was achieved by immobilizing T-PMIA/Ag@RGO NNM in a cross-flow filtration system (shown in Fig. 2). A peristaltic pump was used to regulate the flow rate of the feed solution during this process. In this process, 4-NP in the feed solution continuously flowed through T-PMIA/Ag@RGO NNM. The reduction reaction of 4-NP occurred under the catalysis of Ag nanoparticles during this process. Moreover, the UV-Vis absorbance spectra of the feed solution were recorded with a time interval at a scanning range of 250–500 nm using the UV-Vis spectrophotometer (TU-1810PC).

3. Results and discussion

3.1 Morphology

The SEM and TEM morphology images of GO, PDA@RGO and Ag@RGO are shown in Fig. 3. As shown in Fig. 3, GO, PDA@RGO nanosheets had a smooth surface and the typical folded structure of two dimension materials. Moreover, there were some PDA particles attached onto the PDA@RGO nanosheet surface. By comparing with GO and PDA@RGO, it can be observed that there were some Ag NPs uniformly distributed on the surface of Ag@RGO nanosheets. The results demonstrated that the Ag@RGO nanocomposite was successfully prepared *via* the mussel-inspired method.

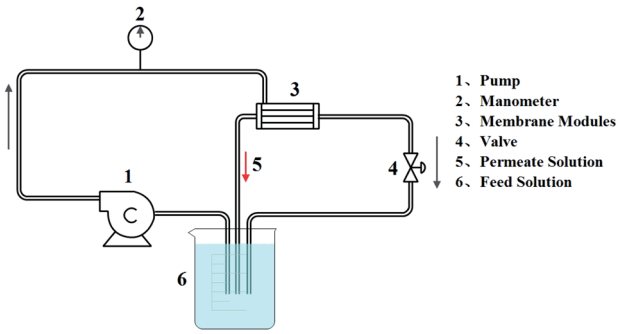

Fig. 2 The schematic of the cross-flow filtration system.

Fig. 4 shows the SEM morphology of T-PMIA/Ag@RGO NNM. T-PMIA/Ag@RGO NNM had a unique tubular shape compared to the flat nanofiber membrane. As shown in Fig. 4(a), the tubular nanofiber membrane was composed of a hollow braided rope and nanofiber layer. The hollow braided rope served as the reinforcement, while the nanofiber layer served as the functional layer. Moreover, the interface bonding between the hollow braided rope and nanofiber layer was good. It was beneficial to improve the mechanical properties of T-PMIA/Ag@RGO NNM. The reinforced mechanism of T-PMIA/Ag@RGO NNM is shown in Fig. S3.† Fig. 4(b) shows the SEM morphology of the nanofiber layer. As shown in Fig. 4(b1), a relatively smooth, uniform and continuous PMIA nanofiber is observed. Fig. 4(b2–b4) show the outer surface morphology of T-PMIA/Ag@RGO NNM. Unlike the morphology of the PMIA nanofiber, the surface of the PMIA/Ag@RGO nanofiber was rough; moreover, a typical two dimensional structure of the Ag@RGO nanocomposite was observed. Moreover, the Ag@RGO nanocomposite was embedded into the nanofiber tightly *via* two junction points, which ensured that the Ag@RGO nanocomposite would not fall off from the PMIA/Ag@RGO nanofibers easily.

In order to further investigate the bonding state of the Ag@RGO nanocomposite and PMIA nanofiber, the TEM morphology of the PMIA/Ag@RGO nanofiber is observed. The result is shown in Fig. 5. The doping of the Ag@RGO nanocomposite is observed clearly in the PMIA/Ag@RGO nanofiber. Moreover, there was no gap between the nanocomposite and nanofibers. This indicated that there was a good combination of the Ag@RGO nanocomposite and PMIA nanofiber. The edge of the Ag@RGO nanocomposite was out of the nanofibers as the size of the Ag@RGO nanocomposite was bigger than the diameter of nanofibers. This was beneficial to increase the contact area between the Ag@RGO nanocomposite and reactants. These provide a structural basis for the application of T-PMIA/Ag@RGO NNM in catalysis.

The Ag loading of T-PMIA/Ag@RGO NNM was detected by EDX. The results are shown in Fig. 6. As shown in Fig. 6, the Ag loading of the PMIA/Ag@RGO composite nanofiber membrane increased considerably when the Ag@RGO content of the electrospining solution increased from 0.2 wt% to 0.6 wt%.

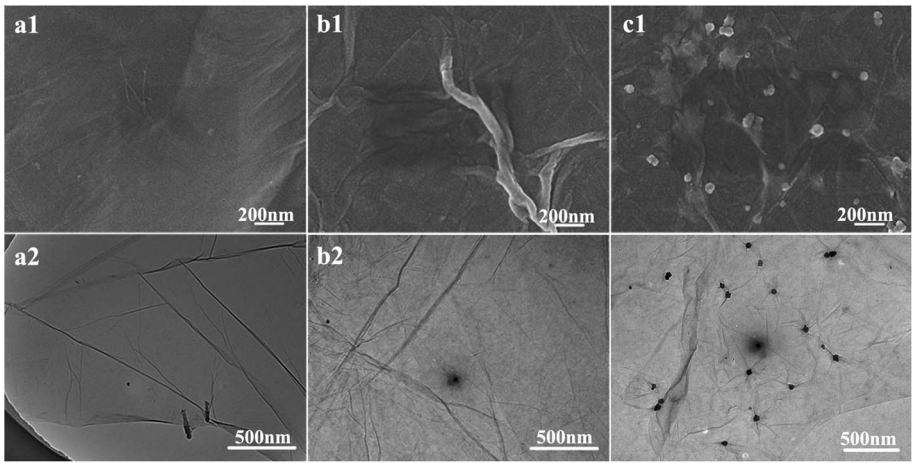

Fig. 3 SEM (1) and TEM (2) morphology images of (a) GO, (b) PDA@RGO, and (c) Ag@RGO.

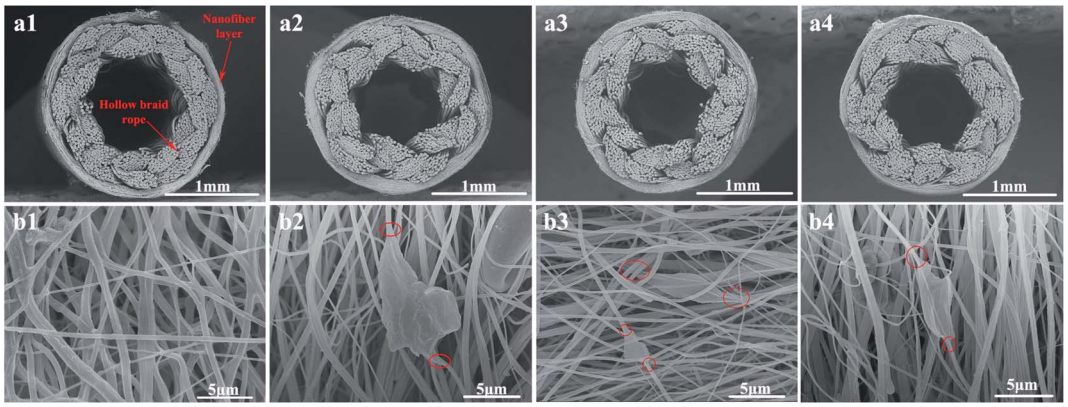

Fig. 4 SEM morphology images of T-PMIA/Ag@RGO NNM (a) cross section and (b) out surface: (1) PMIA, (2) PMIA/Ag@RGO0.2, (3) PMIA/Ag@RGO0.6, and (4) PMIA/Ag@RGO1.0.

However, the Ag loading of the PMIA/Ag@RGO composite nanofiber membrane increased slightly when the Ag@RGO content further increased to 1.0 wt%. The viscosity of the electrospining solution increased with an increase in the Ag@RGO content. This would make the electrospining process to become more and more difficult. Moreover, the electrical conductivity of Ag@RGO was better than that of the PMIA solution. This would not make some Ag@RGO nanocomposites embed into the nanofiber during the electrospinning process. Therefore, the Ag loading of the PMIA/Ag@RGO composite nanofiber membrane increased slightly when the Ag@RGO content further increased to 1.0 wt%.

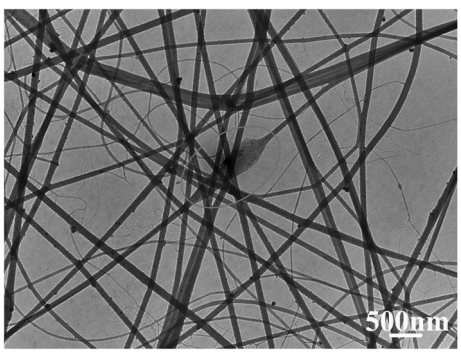

Fig. 5 The TEM morphology of T-PMIA/Ag@RGO NNM.

3.2 Physicochemical characterizations

In order to investigate the chemical composition and elemental state of the samples, the XPS analysis was performed on various samples. The results are shown in Fig. 7. Fig. 7(a) shows the wide scan XPS spectra of the Ag@RGO nanocomposite, PMIA nanofiber and PMIA/Ag@RGO0.6 composite nanofiber membrane. The XPS survey confirms the C, O, N and Ag composition of the Ag@RGO nanocomposite and PMIA/Ag@RGO nanofibers, while there are only C, O and N peaks detected in the PMIA nanofiber. The high resolution Ag3d XPS spectra of the Ag@RGO nanocomposite are shown in Fig. 7(b). The binding energies of $Ag3d_{5/2}$ and $Ag3d_{3/2}$ are 368 eV and 374 eV, respectively, which are the characteristic peaks of Ag^0 species. This indicated that the Ag^+ ions were completely reduced to the Ag^0 state by the PDA layer of PDA@RGO. The

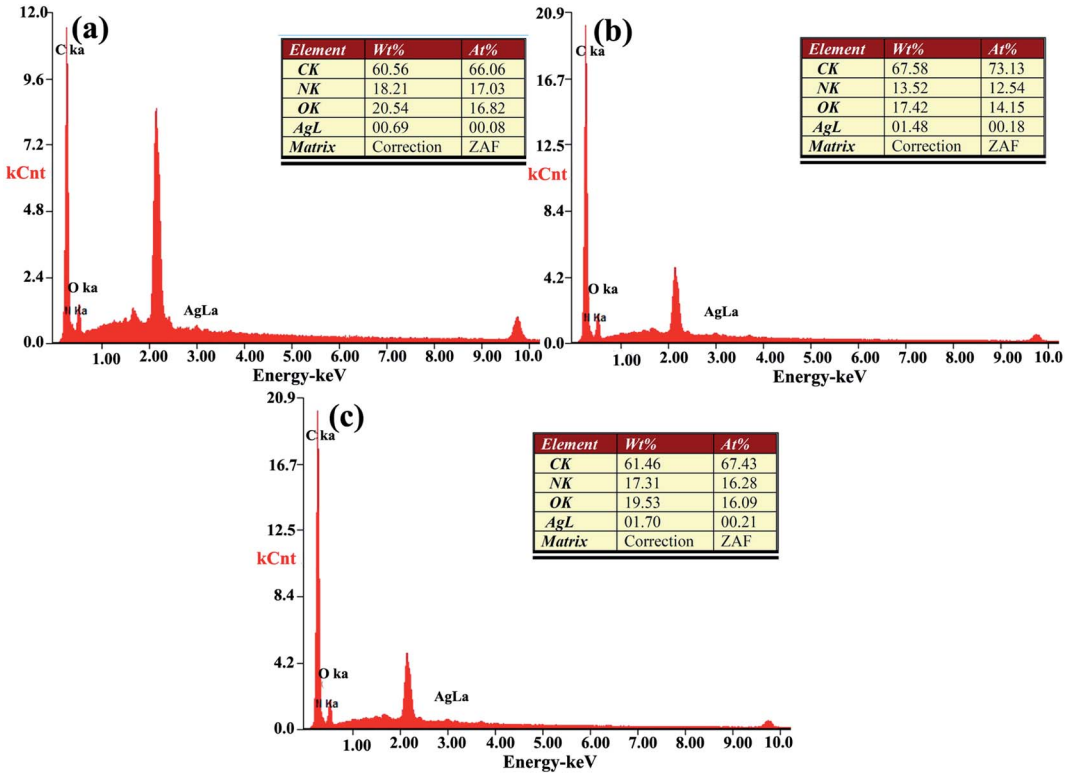

Fig. 6 The EDX spectra of T-PMIA/Ag@RGO NNM: (a) PMIA/Ag@RGO0.2, (b) PMIA/Ag@RGO0.6, and (c) PMIA/Ag@RGO1.0.

surface elemental composition of numerous samples is shown in Table 2. The silver atomic relative contents of the Ag@RGO nanocomposites and PMIA/Ag@RGO0.6 nanofiber are 2.18% and 0.82%, respectively. The results further demonstrated that the Ag@RGO nanocomposites are successfully prepared and embedded into the PMIA/Ag@RGO nanofiber in this study.

The crystal structure of the samples was determined *via* XRD. The XRD patterns of samples are shown in Fig. 7(c). As shown in Fig. 7(c), a typical characteristic peak at about 10° is observed in the GO XRD pattern. However, the peak is not seen in the Ag@RGO nanocomposite, indicating that GO was reduced by PDA. Besides, the XRD pattern of the Ag@RGO nanocomposite showed two new peaks at 38.1° and 44.2°, which correspond to the (111) and (200) lattice planes of Ag nanoparticles, respectively. The same peaks are also present in the PMIA/Ag@RGO nanofiber membrane. This further indicated that the Ag@RGO nanocomposites were embedded into the PMIA/Ag@RGO nanofiber successfully.

3.3 Mechanical property

It was known to all that the mechanical property of the nanofiber membrane was relatively poor, which significantly restricted the applications of the nanofiber membrane. Unlike the general nanofiber membrane, T-PMIA/Ag@RGO NNM showed a superior mechanical property due to the reinforcement of the hollow braided rope. The mechanical property of T-PMIA/Ag@RGO NNM is shown in Fig. 8. As shown in Fig. 8(a), T-PMIA/Ag@RGO NNM could facilely load 1000 g, showing a superior mechanical property, which was important for the applications of T-PMIA/Ag@RGO NNM. Fig. 8(b) shows the compressive property of T-PMIA/Ag@RGO NNM. It was satisfying that the compressive property of T-PMIA/Ag@RGO NNM was also excellent. T-PMIA/Ag@RGO NNM could withstand 500 g without any compression. Therefore, T-PMIA/Ag@RGO NNM could be applied towards a wide range of potential applications without being restricted by the poor mechanical properties of the nanofiber membrane.

3.4 Catalysis performance

As discussed in Fig. 6, the Ag loading of the PMIA/Ag@RGO nanofiber membrane increased slightly when the Ag@RGO content increased from 0.6 wt% to 1.0 wt%. Moreover, the pore size of the tubular PMIA/Ag@RGO0.6 composite nanofiber membrane was bigger than that of the tubular PMIA/Ag@RGO1.0 composite nanofiber membrane (shown in Fig. S4†). Therefore, the tubular PMIA/Ag@RGO0.6 composite nanofiber membrane was chosen to investigate the catalysis performance.

To evaluate the catalytic performance of the tubular PMIA/Ag@RGO0.6 composite nanofiber membrane, the tubular PMIA/Ag@RGO0.6 composite nanofiber membrane was employed for the catalysis of a model reaction for the reduction of 4-NP to 4-AP. The reaction followed pseudo-first order reaction kinetics as the concentration of $NaBH_4$ in the feed solution was higher than 4-NP during the process. Thus, the apparent rate constants (k_{app}) of the reactions could be calculated by the following equation:

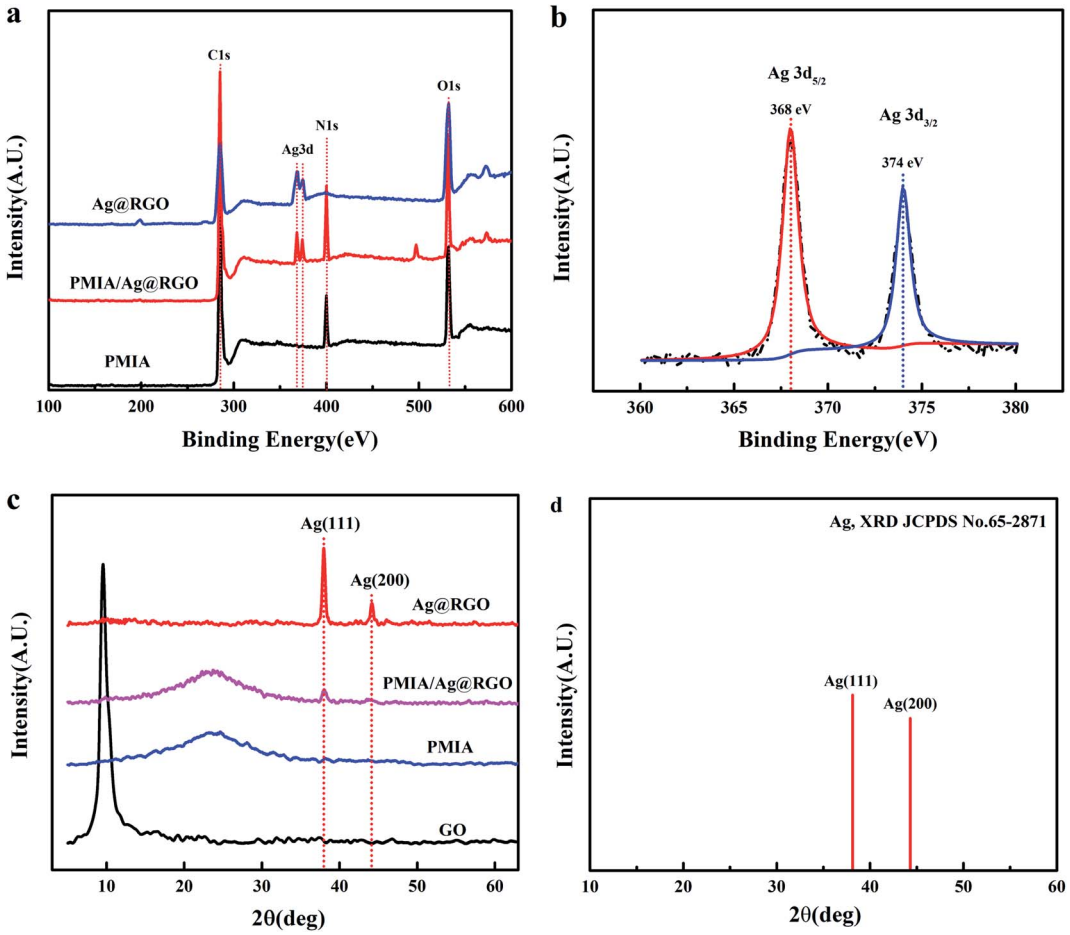

Fig. 7 The XPS spectra of numerous samples (a) wide scan and (b) high resolution of Ag3d; the XRD patterns of various samples (c, d).

Table 2 Surface elemental composition of Ag@RGO nanocomposites and PMIA/Ag@RGO0.6 nanofiber membranes

Sample	C (At%)	O (At%)	N (At%)	Ag (At%)
Ag@RGO	66.41	28	3.42	2.18
PMIA/Ag@RGO0.6	73.29	14.78	11.11	0.82

$$\ln\left(\frac{C_t}{C_0}\right) = -k_{app}t \quad (1)$$

where C_t and C_0 are the concentration values at reaction time (t) and the initial concentration of 4-NP in the feed solution, respectively.

First, the reaction process was carried out with different $NaBH_4$ contents under 0.1 MPa *via* the continuous catalysis model. The volume of the feed solution was 500 ml, which contained 5 mg 4-NP and different contents of $NaBH_4$. The result is shown in Fig. 9(a). As shown in Fig. 9(a), k_{app} increases as the $NaBH_4$ content increases. It was obvious that the increase in the $NaBH_4$ content improved the catalytic performance of the tubular PMIA/Ag@RGO0.6 composite nanofiber membrane. During the reaction process, $NaBH_4$ ionized in water to offer BH_4^-, which would be adsorbed on the Ag@RGO nanocomposite surface; then, the silver nanoparticles started the catalytic reaction by relaying electrons from the donor BH_4^- to the acceptor 4-NP. The increase of the $NaBH_4$ content would donate more electrons which lead to accelerate metal-catalyzed nitroarene hydrogenation. Therefore, the k_{app} of 4-NP to 4-AP conversion increased with the increase in the $NaBH_4$ content. When the addition amount of $NaBH_4$ was 1 g, the mass ratio of $NaBH_4$ and 4-NP had reached 200 : 1; moreover, the increasing trend of k_{app} slowed down when the addition amount of increased from 0.5 g to 1 g. Hence, the addition of $NaBH_4$ was 1 g in the following experiments.

Fig. 9(b) shows the effects of the operating pressure on the catalytic performance of the tubular PMIA/Ag@RGO0.6 composite nanofiber membrane. It was obvious that k_{app} increased as the operating pressure increased. The increase in the operating pressure was beneficial to improve the flow rate of the feed solution. Also, this could facilitate the contact between the catalyst and reactants, as well as the mass transfer. Moreover, k_{app} increased slightly when the operating pressure increased from 0.1 MPa to 0.15 MPa. Based on the above-mentioned results, 0.1 MPa was selected as the operating pressure in subsequent experiments.

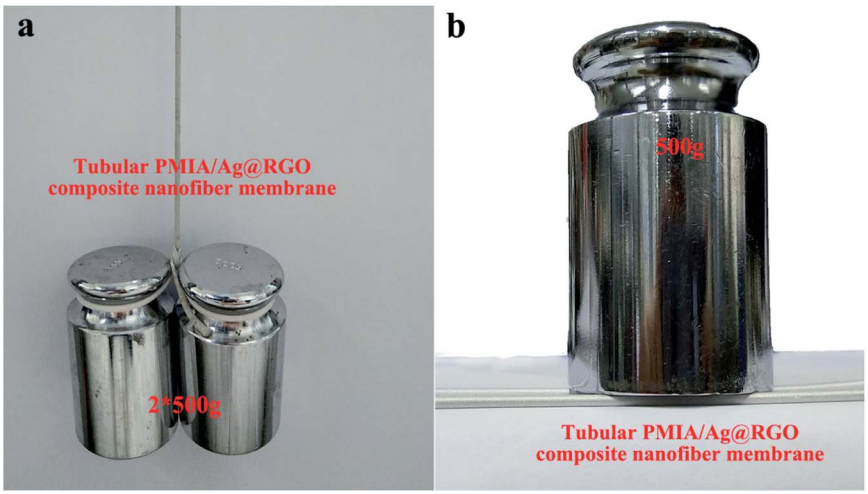

Fig. 8 The mechanical property of T-PMIA/Ag@RGO NNM (a) tensile strength and (b) compressive property.

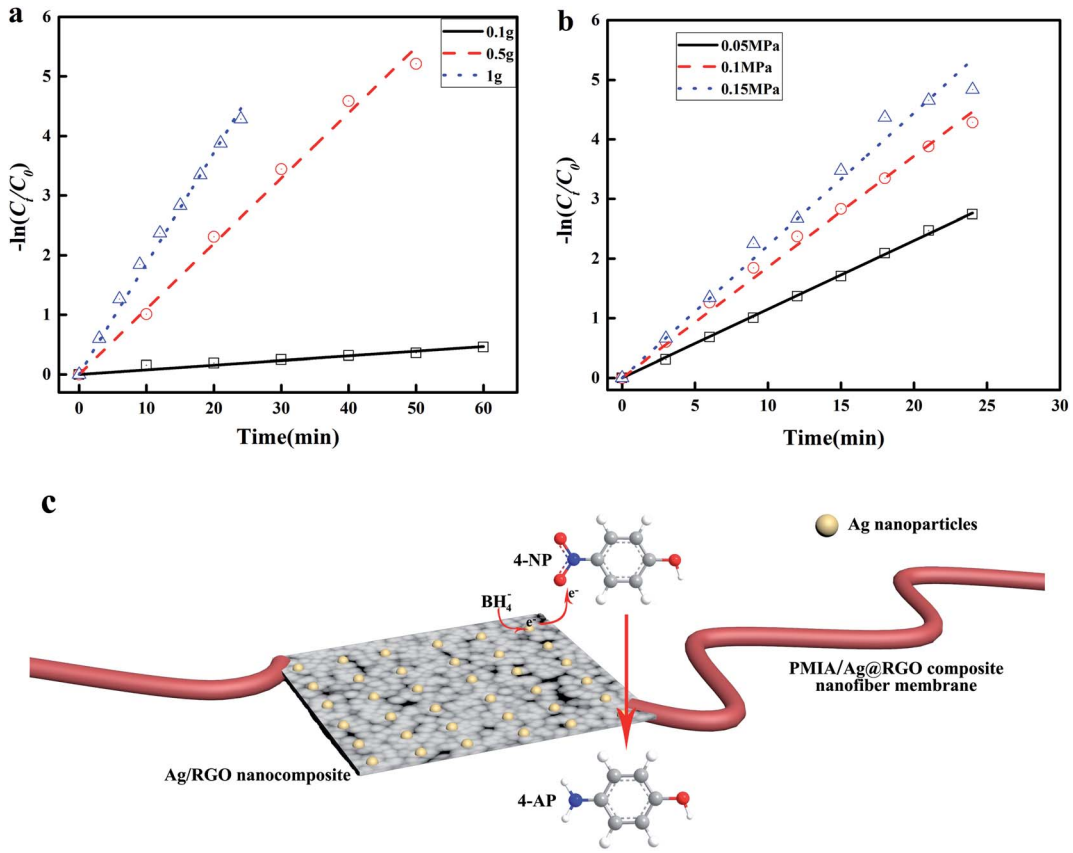

Fig. 9 The effect of operating conditions on the catalytic performance of the tubular PMIA/Ag@RGO0.6 composite nanofiber membrane (a) $NaBH_4$ content, (b) operating pressure, the catalytic reduction mechanism of 4-NP (c).

In order to validate the excellent catalytic performance of the tubular PMIA/Ag@RGO0.6 composite nanofiber membrane, the following experiments were carried out. The results are shown in Fig. 10. First, the catalytic experiment was carried out *via* the continuous catalysis model in the presence of the tubular PMIA/PDA@RGO0.6 composite nanofiber membrane. As shown in Fig. 10(a), the UV-Vis absorption spectra of the feed solution barely changed during this process. The slightly change was probably caused by the adsorption of the tubular PMIA/PDA@RGO0.6 composite nanofiber membrane. Second, the catalytic experiment was carried out *via* the static catalysis model in the presence of the tubular PMIA/Ag@RGO0.6 composite nanofiber membrane. As shown in Fig. 10(b), the UV-Vis absorption spectra of the feed solution at 400 nm

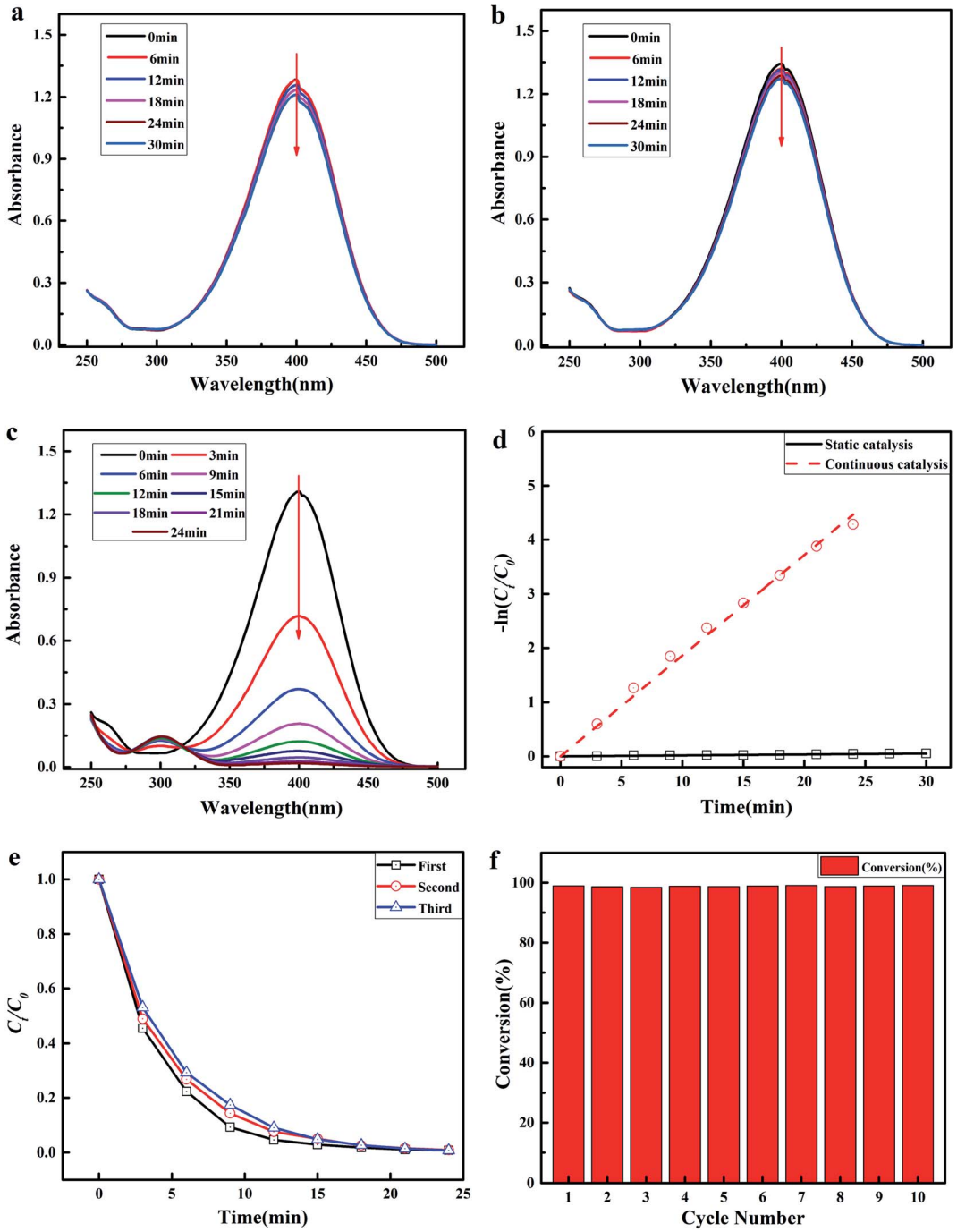

Fig. 10 Time-dependent UV-Vis absorption spectra of the feed solution under different conditions: (a) continuous catalysis process in the presence of the tubular PMIA/PDA@RGO0.6 composite nanofiber membrane; (b) static catalysis process in the presence of the tubular PMIA/Ag@RGO0.6 composite nanofiber membrane; (c) continuous catalysis process in the presence of the tubular PMIA/Ag@RGO0.6 composite nanofiber membrane. (d) $-\ln(C_t/C_0)$ *versus* reaction time in the presence of the tubular PMIA/Ag@RGO0.6 composite nanofiber membrane. Catalytic activity (e) and conversion rate of 4-NP (f) during the cyclic test of the continuous catalysis process.

decreased slightly. It demonstrated that a few 4-NPs in the feed solution was transferred to 4-AP during the static catalysis process as the presence of the tubular PMIA/Ag@RGO0.6 composite nanofiber membrane. Alternatively, the reaction efficiency of 4-NP to 4-AP was very low under this condition. In such a situation, the contact probability between the catalyst and reactants was very low. Therefore, the catalytic reaction of 4-NP to 4-AP could not be carried out efficiently. As discussed above, the T-PMIA/Ag@RGO NNM had a superior mechanical property. Therefore, the catalytic test could be carried out *via* the continuous catalysis model. The result is shown in Fig. 10(c). It was obvious that the UV–Vis absorption spectra of

the feed solution at 400 nm had fallen rapidly during the continuous catalysis process. It indicated that 4-NP was rapidly transferred to 4-AP during the continuous catalysis process. The k_{app} values of the static and continuous catalysis processes were calculated based on the slope of the fitted lines, as shown in Fig. 10(d). The k_{app} values were 1.86×10^{-1} min^{-1} and 1.76×10^{-3} min^{-1} for continuous and static catalysis processes, respectively. The k_{app} of the continuous catalysis process was 105.7 times higher than the static catalysis process as the mass transfer rate in the continuous catalysis process was much higher than that of the static catalysis process. A much faster mass transport in the continuous catalysis process was beneficial to bring 4-NP to Ag nanoparticles surface and remove 4-AP from the reaction zone during the continuous catalysis process. This is responsible to the higher catalytic activity in the continuous catalysis process. However, most nanofiber membranes could only be used under this condition due to its poor mechanical properties. The results further demonstrated the superiority of the tubular PMIA/Ag@RGO0.6 composite nanofiber membrane due to its excellent mechanical property and unique construction.

The catalytic stability is also a key point for the application of the tubular PMIA/Ag@RGO0.6 composite nanofiber membrane. Therefore, the catalytic stability of the tubular PMIA/Ag@RGO0.6 composite nanofiber membrane was studied. The results are shown in Fig. 10(e, f). As shown in Fig. 10(e), the catalytic activity had merely changed after three cycles. Moreover, the conversion of 4-NP was almost constant during ten cycles, as shown in Fig. 10(f). These results indicated that the tubular PMIA/Ag@RGO0.6 composite nanofiber membrane had a good catalytic stability. As discussed above, there was a good combination of the Ag@RGO nanocomposite and PMIA nanofiber; moreover, the Ag nanoparticles adhered well to the Ag@RGO nanocomposite surface. These could ensure that the catalysts would not fall off from the tubular PMIA/Ag@RGO0.6 composite nanofibers easily during the continuous catalysis process and made it easy for the recycling of catalysts.

4. Conclusion

In conclusion, we developed a simple and facile method for the fabrication of T-PMIA/Ag@RGO NNM with superior mechanical property, highly recyclable and good catalytic efficiency towards the reduction of 4-NP. The special tubular shape and superior mechanical property enabled it to be used in the continuous catalysis process. The k_{app} value of the continuous catalysis process was 105.7 times higher than that of the static catalysis process in the presence of the tubular PMIA/Ag@RGO0.6 composite nanofiber membrane. Moreover, T-PMIA/Ag@RGO NNM showed good catalytic stability and recyclability as the Ag@RGO nanocomposite and PMIA nanofiber had a good binding state. In consideration of its simplicity and generality, this strategy showed a great potential for improving the poor mechanical property of the nanofiber membrane and expanding its application for catalytic transformation in the field of environmental remediation.

Conflicts of interest

There are no conflicts to declare.

Acknowledgements

This work was supported by the National Natural Science Foundation of China (21808165), the start-up funding from Hebei University of Science and Technology (1181368), the Key Research and Development Project of Hebei Province (20271202D).

References

1 N. Liu, W. Zhang, X. Li, R. Qu, Q. Zhang, Y. Wei, L. Feng and L. Jiang, *J. Mater. Chem.*, 2017, **5**, 15822–15827.
2 Y. Xu, X. Shi, R. Hua, R. Zhang, Y. Yao, B. Zhao, T. Liu, J. Zheng and G. Lu, *Appl. Catal., B*, 2020, **260**, 118142.
3 X. Fang, J. Li, B. Ren, Y. Huang, D. Wang, Z. Liao, Q. Li, L. Wang and D. D. Dionysiou, *J. Membr. Sci.*, 2019, **579**, 190–198.
4 T. Cai, G. Fang, X. Tian, J.-J. Yin, C. Chen and C. Ge, *ACS Nano*, 2019, **13**, 12694–12702.
5 M. Rafique, I. Sadaf, M. B. Tahir, M. S. Rafique, G. Nabi, T. Iqbal and K. Sughra, *Mater. Sci. Eng., C*, 2019, **99**, 1313–1324.
6 Q. Wu, G.-E. Chen, W.-G. Sun, Z.-L. Xu, Y.-F. Kong, X.-P. Zheng and S.-J. Xu, *Chem. Eng. J.*, 2017, **313**, 450–460.
7 D. Costa, J. Oliveira, M. S. Rodrigues, J. Borges, C. Moura, P. Sampaio and F. Vaz, *Appl. Surf. Sci.*, 2019, **496**, 143701.
8 R. Cheng, T. Hu, M. Hu, C. Li, Y. Liang, Z. Wang, H. Zhang, M. Li, H. Wang, H. Lu, Y. Fu, H. Zhang, Q.-H. Yang and X. Wang, *J. Mater. Sci. Technol.*, 2020, **40**, 119–127.
9 E. Stankevičius, E. Daugnoraitė, I. Ignatjev, Z. Kuodis, G. Niaura and G. Račiukaitis, *Appl. Surf. Sci.*, 2019, **497**, 143752.
10 L. Zhao, C. Deng, S. Xue, H. Liu, L. Hao and M. Zhu, *Chem. Eng. J.*, 2020, **402**, 126223.
11 Y. Li, P. Zhang, Z. Ouyang, M. Zhang, Z. Lin, J. Li, Z. Su and G. Wei, *Adv. Funct. Mater.*, 2016, **26**, 2122–2134.
12 X. Lou, C. Zhu, H. Pan, J. Ma, S. Zhu, D. Zhang and X. Jiang, *Electrochim. Acta*, 2016, **205**, 70–76.
13 H. Hu, J. H. Xin and H. Hu, *J. Mater. Chem.*, 2014, **2**, 11319–11333.
14 X. An, Y. Long and Y. Ni, *Carbohydr. Polym.*, 2017, **156**, 253–258.
15 P. Kumar Sahoo, B. Panigrahy, D. Thakur and D. Bahadur, *New J. Chem.*, 2017, **41**, 7861–7869.
16 Z. Ji, Y. Wang, X. Shen, H. Ma, J. Yang, A. Yuan and H. Zhou, *J. Colloid Interface Sci.*, 2017, **487**, 223–230.
17 X. Liu, Q. Han, Y. Zhang, X. Wang, S. Cai, C. Wang and R. Yang, *Appl. Surf. Sci.*, 2019, **471**, 929–934.
18 B. P. Upoma, F. Mahnaz, W. Rahman Sajal, N. Zahan, M. S. Hossain Firoz and M. S. Azam, *J. Environ. Chem. Eng.*, 2020, **8**, 103739.
19 A. Dhakshinamoorthy, A. M. Asiri and H. Garcia, *ACS Catal.*, 2017, **7**, 2896–2919.

20 J. Han, J. Cho, J.-C. Kim and R. Ryoo, *ACS Catal.*, 2018, **8**, 876–879.
21 Y. Han, H. Xu, Y. Su, Z.-l. Xu, K. Wang and W. Wang, *J. Catal.*, 2019, **370**, 70–78.
22 B. Zahed and H. Hosseini-Monfared, *Appl. Surf. Sci.*, 2015, **328**, 536–547.
23 H. Abadikhah, E. Naderi Kalali, S. Khodi, X. Xu and S. Agathopoulos, *ACS Appl. Mater. Interfaces*, 2019, **11**, 23535–23545.
24 X. Yang, P. Pachfule, Y. Chen, N. Tsumori and Q. Xu, *Chem. Commun.*, 2016, **52**, 4171–4174.
25 Y. Chen, Q.-L. Zhu, N. Tsumori and Q. Xu, *J. Am. Chem. Soc.*, 2015, **137**, 106–109.
26 L. T. Soo, K. S. Loh, A. B. Mohamad, W. R. W. Daud and W. Y. Wong, *J. Power Sources*, 2016, **324**, 412–420.
27 B. Wang, T.-y. Chang, Z. Jiang, J.-j. Wei, Y.-h. Zhang, S. Yang and T. Fang, *Int. J. Hydrogen Energy*, 2018, **43**, 7317–7325.
28 L. Guo, Q. Liu, G. Li, J. Shi, J. Liu, T. Wang and G. Jiang, *Nanoscale*, 2012, **4**, 5864–5867.
29 W. Ye, J. Yu, Y. Zhou, D. Gao, D. Wang, C. Wang and D. Xue, *Appl. Catal., B*, 2016, **181**, 371–378.
30 F. Ren, C. Zhai, M. Zhu, C. Wang, H. Wang, D. Bin, J. Guo, P. Yang and Y. Du, *Electrochim. Acta*, 2015, **153**, 175–183.
31 E. Yang, A. B. Alayande, C.-M. Kim, J.-h. Song and I. S. Kim, *Desalination*, 2018, **426**, 21–31.
32 X. Xu, Q. Zheng, G. Bai, L. Song, Y. Yao, X. Cao, S. Liu and C. Yao, *Electrochim. Acta*, 2017, **242**, 56–65.
33 J. Wang, H. Guo, Z. Yang, Y. Mei and C. Y. Tang, *J. Membr. Sci.*, 2017, **525**, 298–303.
34 L. Miao, G. Liu and J. Wang, *ACS Appl. Mater. Interfaces*, 2019, **11**, 7397–7404.
35 J. Wang, X. Pei, G. Liu, J. Bai, Y. Ding, J. Wang and F. Liu, *J. Colloid Interface Sci.*, 2019, **538**, 108–115.
36 Z. Zhang, Y. Yang, C. Li and R. Liu, *J. Membr. Sci.*, 2019, **582**, 350–357.
37 D. Hu, Y. Huang, H. Liu, H. Wang, S. Wang, M. Shen, M. Zhu and X. Shi, *J. Mater. Chem.*, 2014, **2**, 2323–2332.
38 M. Gopiraman, H. Bang, G. Yuan, C. Yin, K.-H. Song, J. S. Lee, I. M. Chung, R. Karvembu and I. S. Kim, *Carbohydr. Polym.*, 2015, **132**, 554–564.
39 A. Celebioglu, Z. Aytac, O. C. O. Umu, A. Dana, T. Tekinay and T. Uyar, *Carbohydr. Polym.*, 2014, **99**, 808–816.
40 A. Celebioglu, F. Topuz, Z. I. Yildiz and T. Uyar, *Carbohydr. Polym.*, 2019, **207**, 471–479.
41 A. Celebioglu, F. Topuz and T. Uyar, *New J. Chem.*, 2019, **43**, 3146–3152.
42 Y. Zhong, T. Li, H. Lin, L. Zhang, Z. Xiong, Q. Fang, G. Zhang and F. Liu, *Chem. Eng. J.*, 2018, **344**, 299–310.
43 Y. Liu, K. Zhang, W. Li, J. Ma and G. J. Vancso, *J. Mater. Chem.*, 2018, **6**, 7741–7748.
44 Z. Zeng, M. Wen, B. Yu, G. Ye, X. Huo, Y. Lu and J. Chen, *ACS Appl. Mater. Interfaces*, 2018, **10**, 14735–14743.
45 L. Zhang, Z. Liu, Y. Wang, R. Xie, X.-J. Ju, W. Wang, L.-G. Lin and L.-Y. Chu, *Chem. Eng. J.*, 2017, **309**, 691–699.
46 H. Lin, Q. Fang, W. Wang, G. Li, J. Guan, Y. Shen, J. Ye and F. Liu, *Appl. Catal., B*, 2020, **273**, 119047.
47 Y. Zhong, S. Mahmud, Z. He, Y. Yang, Z. Zhang, F. Guo, Z. Chen, Z. Xiong and Y. Zhao, *J. Hazard. Mater.*, 2020, **397**, 122774.
48 Z. Wang, X. Chen, K. Li, S. Bi, C. Wu and L. Chen, *J. Membr. Sci.*, 2015, **496**, 95–107.
49 M. Chen, C. Xiao, C. Wang, H. Liu, H. Huang and D. Yan, *Nanoscale*, 2018, **10**, 19835–19845.
50 X. Wang, C. Xiao, H. Liu, M. Chen, H. Xu, W. Luo and F. Zhang, *J. Membr. Sci.*, 2020, **596**, 117583.
51 H. Zhao, W. Kang, N. Deng, M. Liu and B. Cheng, *Chem. Eng. J.*, 2020, **384**, 123312.
52 L. Zhong, T. Wang, L. Liu, W. Du and S. Wang, *Sep. Purif. Technol.*, 2018, **202**, 357–364.
53 N. Deng, Y. Wang, J. Yan, J. Ju, Z. Li, L. Fan, H. Zhao, W. Kang and B. Cheng, *J. Power Sources*, 2017, **362**, 243–249.